Deriving High-Resolution Urban Air Pollution Maps Using Mobile Sensor Nodes

David Hasenfratz[a,*], Olga Saukh[a], Christoph Walser[a], Christoph Hueglin[b], Martin Fierz[c], Tabita Arn[a], Jan Beutel[a], Lothar Thiele[a]

[a] *Computer Engineering and Networks Laboratory, ETH Zurich, Switzerland*
[b] *Laboratory for Air Pollution and Environmental Technology, EMPA, Switzerland*
[c] *Institute for Aerosol and Sensor Technology, FHNW, Switzerland*

Abstract

Up-to-date information on urban air pollution is of great importance, *e.g.*, for environmental protection agencies to assess air quality and provide advice to the general public in a timely manner. In particular, ultrafine particles (UFPs) are widely spread in urban environments and may have a severe impact on human health. However, the lack of knowledge about the spatio-temporal distribution of UFPs hampers profound evaluation of these effects. In this paper, we analyze one of the largest spatially resolved UFP data set publicly available today containing over 50 million measurements. We collected the measurements throughout more than two years using mobile sensor nodes installed on top of public transport vehicles in the city of Zurich, Switzerland. Based on these data, we develop land-use regression models to create pollution maps with a high spatial resolution of 100 m $\times$ 100 m. We compare the accuracy of the derived models across various time scales and observe a rapid drop in accuracy for maps with sub-weekly temporal resolution. To address this problem, we propose a novel modeling approach that incorporates past measurements annotated with metadata into the modeling process. In this way, we achieve a 26 % reduction in the root-mean-square error—a standard metric to evaluate the accuracy of air quality models—of pollution maps with semi-daily temporal resolution. We believe that our findings can help epidemiologists to better understand the adverse health effects related to UFPs and serve as a stepping stone towards detailed real-time pollution assessment.

Keywords: Mobile sensor network, Air pollution, Land-use regression, High-resolution pollution maps, Ultrafine particles, Health-optimal routing

1. Introduction

Air pollution is a major concern in many cities worldwide. Atmospheric pollutants considerably affect human health; they are responsible for a variety of respiratory and cardiovascular diseases and are known to cause cancer if humans are exposed to them for extended periods of time [1]. Additionally, air pollution is responsible for environmental problems, such as eutrophication and acidification of ecosystems.

*Corresponding author. Tel.: +41 446327067.
Email address: hasenfratz@tik.ee.ethz.ch (David Hasenfratz)

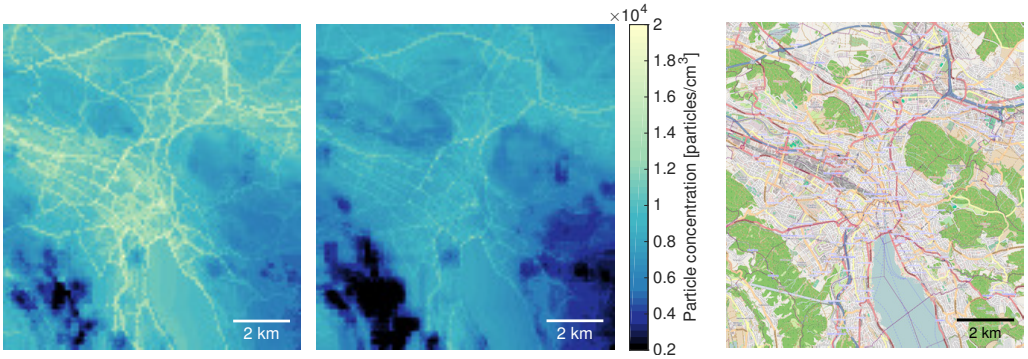

(a) Monday–Saturday. (b) Sunday. (c) Map of Zurich.

Figure 1: Novel ultrafine particle concentration maps for Zurich (Switzerland). The particle concentrations are higher during the week (Monday–Saturday) than on weekends (Sunday) due to higher traffic volumes.

Most countries have mass emission limits for particulate matter PM_{10} and $PM_{2.5}$ (*i.e.*, particles with a diameter of less than 10 µm and 2.5 µm, respectively), but have no restrictions on ultrafine particles (UFPs). UFPs are particles with a diameter of less than 100 nm. In ambient air, UFPs are mainly man-made as byproducts of specific high temperature processes, such as combustion reactions in car engines. The adverse health effects of UFPs are most probably underestimated when they are traditionally monitored by mass as part of PM_{10} and $PM_{2.5}$ [2]. This is because UFPs make a dominant contribution to the total number of urban particle concentrations, but their contribution to the total particle mass is small [3]. Therefore, UFPs were not considered particularly hazardous in the past. There are strong indications, however, that adverse health effects are more related to particle number concentration rather than to particle mass [2]. To better understand the adverse health effects of UFPs, it is essential to have spatially resolved UFP concentration measurements at hand [4].

Nowadays, air pollution is monitored by networks of static measurement stations operated by official authorities. These stations are highly reliable and able to accurately measure a wide range of air pollutants. However, their high acquisition and maintenance costs severely limit the number of installations. As a result, very little is known about the spatial distribution of air pollutants in urban environments and there is a lack of accurate intraurban air pollution maps. However, for air pollutants with high spatial variability, such as UFPs, the public availability of reliable pollution maps is essential. They raise the citizens' awareness about air pollution and empower environmental scientists to craft and evaluate new policies.

Contributions and road-map. To tackle the challenges above, we propose to use a mobile measurement system [5, 6, 7, 8]. Node mobility trades off temporal resolution against spatial resolution, enabling a high spatial resolution across large areas without the need for a huge number of fixed sensors. However, due to the reduced temporal resolution of any covered location, it is a formidable challenge to derive pollution maps with a high temporal resolution at daily or hourly time scales. In this paper, we demonstrate that a mobile measurement system can effectively be used to derive accurate UFP pollution maps with high spatio-temporal resolution.

Our mobile measurement system consists of ten sensor nodes installed on top of public transport vehicles, which cover a large urban area on a regular schedule. The sensor nodes are equipped with a novel measurement device (MiniDiSCs [9]) to monitor UFP concentrations.

Throughout more than two years, we collected over 50 million UFP measurements. Based on these data, we develop land-use regression (LUR) models to produce accurate pollution maps with high spatio-temporal resolution, such as those depicted in Fig. 1. LUR models use a set of explanatory variables (land-use and traffic data) to model pollution concentrations at locations not covered by the mobile sensor nodes. In a first step, we evaluate the dependencies between the explanatory variables and the measurements. Then, we exploit these relationships to predict the pollution levels for all locations without measurements but with available land-use and traffic information. Using this method and our mobile measurement system, we derive accurate and fine-grained pollution maps, which are valuable to environmental scientists, epidemiologists, and the general public. Finally, we use the developed pollution maps to analyze how much urban dwellers from Zurich (Switzerland) can reduce their exposure to UFPs by not taking the shortest path between origin and destination but a healthier and slightly longer alternative route.

In summary, this paper makes the following contributions:

- We introduce in Sec. 2 our mobile measurement system, which is deployed in the city of Zurich (Switzerland) collecting a highly spatially resolved data set of UFP measurements. From April 2012 to April 2014, we collected more than 50 million UFP measurements.
- Assessing the quality of the measurements is difficult due to very sparse ground truth data. We post-process the measurements (calibration and filtering) and propose in Sec. 3 a three-fold validation approach to evaluate the quality of the processed data. Our analysis indicates a high data quality.
- We use the validated measurements in Sec. 4 to derive LUR models for UFP pollution maps with a high spatial resolution of $100\,\mathrm{m} \times 100\,\mathrm{m}$. In Sec. 5 we apply standard metrics to analyze the quality of the models from yearly up to semi-daily temporal resolutions. We find a good quality of pollution maps with yearly to weekly time scales, while models with sub-weekly temporal resolutions perform less well.
- To tackle this problem, we propose in Sec. 6 a novel modeling approach that incorporates past measurements (annotated with metadata, such as environmental and meteorological conditions) into the modeling process. In this way, we increase the quality of pollution maps with a high temporal resolution. For example, we decrease the root-mean-square error—a standard metric to evaluate the accuracy of air quality models—of semi-daily pollution maps by 26 %.
- We use the pollution maps derived to enable a novel route planner application. We show in Sec. 7 that city dwellers can reduce their exposure to UFPs by 7 % on average by not walking along the shortest path between two locations in the city but pursuing a slightly longer healthier path, which minimizes the expected exposure to UFPs.

Using our measurement system and modeling approach, we create UFP pollution maps with an accuracy that is comparable to state-of-the-art air pollution maps, while achieving unprecedented spatio-temporal resolution [10]. We survey related work in Sec. 8, and conclude in Sec. 9.

2. Mobile Air Pollution Monitoring System

Starting in 2012, we gradually equipped ten streetcars of the public transport network in Zurich, Switzerland, with air quality measurement stations as part of the OpenSense project [11, 8], as shown in Fig. 2(a). The sensor nodes cover a large urban area of $100\,\mathrm{km}^2$ on a regular schedule and monitor a wide range of air pollutants and environmental parameters. The

(a) Streetcar with sensor node on top (red circle).

(b) Inner view of the air quality sensor node.

Figure 2: The air quality sensor nodes are installed on top of streetcars. The sensor nodes are equipped with UFP, CO, O_3, and NO_2 sensors. Geotagged and time-stamped measurements are transmitted over GSM (cellular network) to the back-end server for further processing.

(a) Inner view.

(b) External view.

Figure 3: Each air intake is equipped with a protection cover to retain water and dust.

measurements are locally stored in a database and transmitted in real-time over GSM (cellular network) to the back-end server running Global Sensor Network (GSN) [12], a software middleware that facilitates data collection in sensor networks. The sensor readings are removed from the local database once their reception is acknowledged by the back-end server. The web-based caching and visualization tool Vizzly [13] displays the measured particle concentrations on top of Google Maps. All measurements are publicly available.[1]

2.1. Air Quality Sensor Node

The core of the sensor node, depicted in Fig. 2(b), is a Gumstix (embedded computer) with a 600 MHz CPU running the Ångström embedded Linux operating system [14]. A GPS receiver from u-blox supplies the station with precise geospatial information. The station supports bidirectional communication over GSM and WiFi on the 2.4 GHz and 5 GHz frequency bands. GSM

[1] `http://www.opensense.ethz.ch`

Table 1: The ten mobile sensor nodes collected a wide range of pollution measurements over the course of two years.

Air pollutant	Number of measurements [in millions]	Sampling interval	Time period
Ultrafine particles (UFPs)	52	5 s	2 years (ongoing)
Surface ozone (O_3)	9	20 s–60 s	2 years (ongoing)
Temperature / Humidity	9	20 s–60 s	2 years (ongoing)
Carbon monoxide (CO)	2	10 s	2 months (ongoing)
Nitrogen dioxide (NO_2)	2	10 s	2 months (ongoing)
RF electromagnetic fields	4	15 s–30 s	4 months (finished)

is used under regular system operation while WiFi is used during debugging and maintenance phases. All radio signals (GPS, GSM, and WiFi) are processed by a single planar antenna, which is mounted on top of the box. While the streetcars are in operation, on average 20 h per day [7], they supply the nodes with power. During the night, typically from 1:00 AM to 5:00 AM, the streetcars are in their depots and the nodes are turned off.

All air intakes are equipped with protection covers, as depicted in Fig. 3. The bottom side of the aluminum cover has multiple air vents and two inclined bars to retain water and dust. The fan on the back of the node draws air out of the box to ensure a steady air flow. To monitor air pollution, the sensor nodes are equipped with a semiconductor-based ozone (O_3) sensor [15], electrochemical-based carbon monoxide (CO) and nitrogen dioxide (NO_2) sensors [16, 17], and a novel compact device to measure UFP concentrations [9]. Additionally, the nodes monitor radio-frequency electromagnetic fields [18] and environmental parameters, such as temperature and humidity [19]. Over the past two years, we collected huge data sets of spatially resolved pollution measurements, as summarized in Table 1. In this work, we focus on analyzing the UFP data set, which is a unique pollution data set comprising by far the largest number of measurements.

2.2. Data Set of Ultrafine Particle (UFP) Concentrations

The sensor nodes are equipped with Miniature Diffusion Size Classifiers (MiniDiSCs) [9] (see Fig. 2(b)), a novel tool for UFP monitoring. Traditionally, airborne particles are monitored by mass, hence UFPs, which appear in high numbers but have low mass, are not well represented, despite their specific adverse health effects [2]. Whereas the MiniDiSC, a compact hand-held device (4 x 9 x 18 cm), is able to monitor particle number concentrations. It can detect concentrations between 10^3–10^6 particles/cm^3, so it embraces the average daily range in urban environments of 10^4–10^5 particles/cm^3.

The functional principle of the MiniDiSC is based on unipolar charging of aerosol particles, followed by detection in two electrometer stages. In short, the particles are first charged in a standard positive unipolar diffusion charger, which imparts an average charge on the particles that is approximately proportional to the particle diameter. The charged particles then flow through a diffusion stage and generate a current, which is dependent on the average particle size and is used to calculate the number of particles per cm^3.

We deployed the first five sensor nodes with integrated MiniDiSCs in April and May 2012 and an additional five devices in January 2013. The MiniDiSCs sample UFP every 50 ms. The measurements are aggregated to one sample per 5 s, to reduce the amount of transmitted data. Each sensor node transmits around 10,000 measurements per day to the back-end infrastructure,

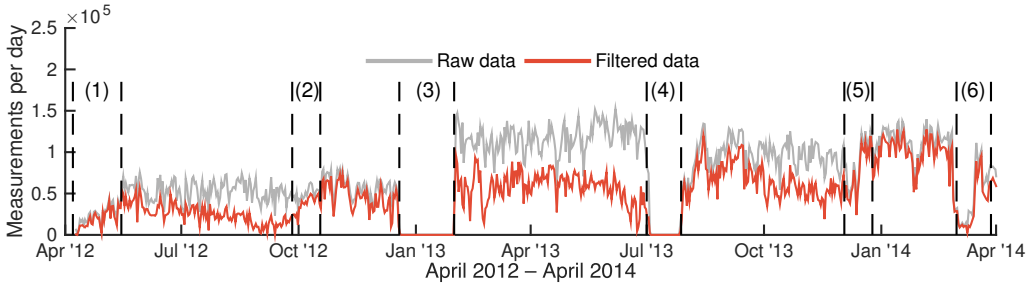

(a) Number of measurements per day across all installed devices.

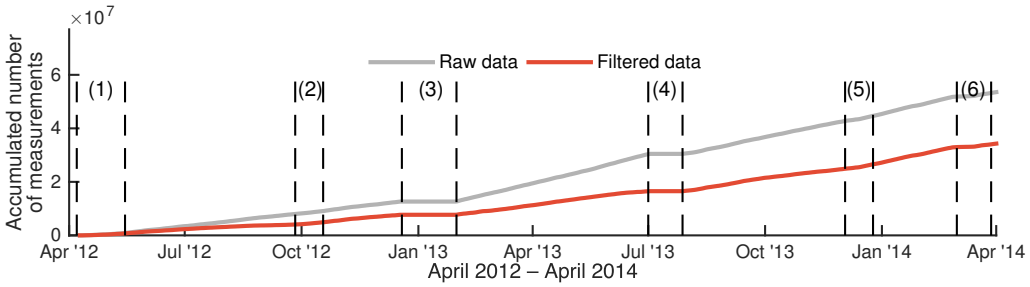

(b) Accumulated number of measurements across all installed devices.

Figure 4: Number of UFP measurements per day and accumulated number of measurements over the course of two years with six service phases (1)–(6).

as depicted in Fig. 4(a) (raw data). In total, we collected over 50 million aggregated measurements, as shown in Fig. 4(b). Further, we depict in Fig. 4 the six main service phases since the start of the deployment: (1) Initial installation of the first five sensor nodes, (2) cleaning of the MiniDiSCs on top of the streetcars (no deinstallation required) to increase data quality, (3) deinstallation of the MiniDiSCs for cleaning and re-calibration, and installation of five additional devices, (4) deinstallation of all devices for cleaning and recalibration, (5) cleaning of the MiniDiSCs on top of the streetcars, and (6) sensor upgrade with new CO and NO_2 sensors.

Offset calibration and filtering of the data. We ensure a high data quality by calibrating and filtering the timestamped and geo-tagged measurements. For one minute in every hour the devices go into a self-calibrating phase to measure their null-offsets, which we use offline to adjust the offset of all measured particle concentrations. Then, we use a two-stage filtering process to remove faulty and unreliable measurements.

First, a GPS-based filter eliminates measurements with horizontal dilution of precision (HDOP) values above three. The HDOP value specifies the GPS location's precision based on the geometric positioning of the GPS satellites. Values below three denote a good to excellent positioning within a few meters. We consider only these measurements, which make up more than 99 % of all measurements.

The second filter examines the internal status variables of the MiniDiSCs, which are transmitted to the back-end server in addition to the particle concentration numbers. These variables allow to draw conclusions about the proper functioning of the devices. We discard measurements if a status variable indicates a malfunction, such as a too low air flow. Additionally, the

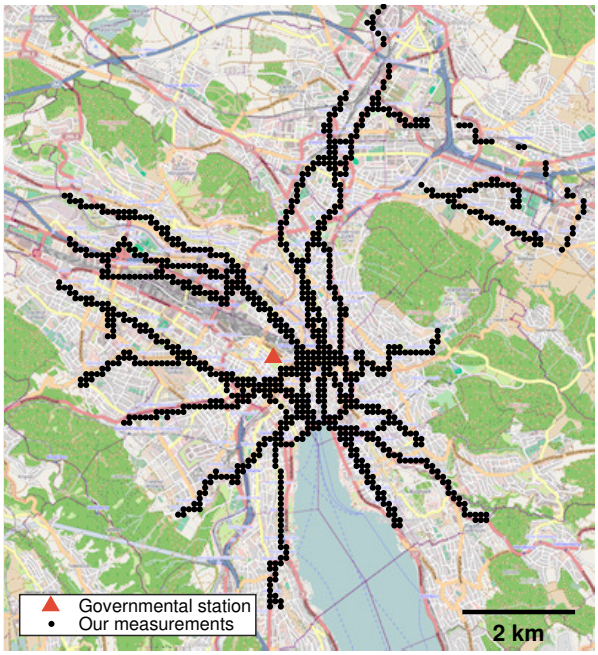

Figure 5: Ten mobile sensor nodes deployed on top of streetcars of the public transport network achieve a good coverage of the city of Zurich (Switzerland). The dots denote locations with at least 50 measurements over the course of two years.

MiniDiSCs need a warm-up phase; therefore, all measurements within one hour after start-up are discarded (the nodes are continuously powered 20 h per day on average). The two-stage filtering process invalidates 36 % of the measurements (mainly the second filter), as shown in Fig. 4. The filtering steps are crucial to achieve high data quality, as we will detail in the next section.

Spatial coverage. A good spatial coverage of the measurements is essential to precisely assess the UFP distribution in urban environments. The spatial coverage of the filtered UFP measurements is shown in Fig. 5. The dots denote locations (100 m $\times$ 100 m) with at least 50 measurements over the course of two years. The ten mobile sensor nodes achieve a good coverage, in particular compared to the single governmental station monitoring UFPs in Zurich, denoted with a triangle in Fig. 5. Our measurements cover a large set of diverse location characteristics. For example, the data set includes measurement locations at terrain elevations from 400–610 m and at diverse traffic densities ranging from vehicle-free zones to areas with over 90,000 vehicles per day.

3. Data Validation

Good data quality is a must for the development of reliable pollution maps. Evaluating the quality of measurements spread over a large urban area is a challenging task, especially if no (or only sparse) ground truth is available [20]. The MiniDiSC has been thoroughly tested in laboratory environment and in the field [9]. However, despite these tests it is unclear whether the harsh deployment setting on top of streetcars has an impact on the quality of the measurements.

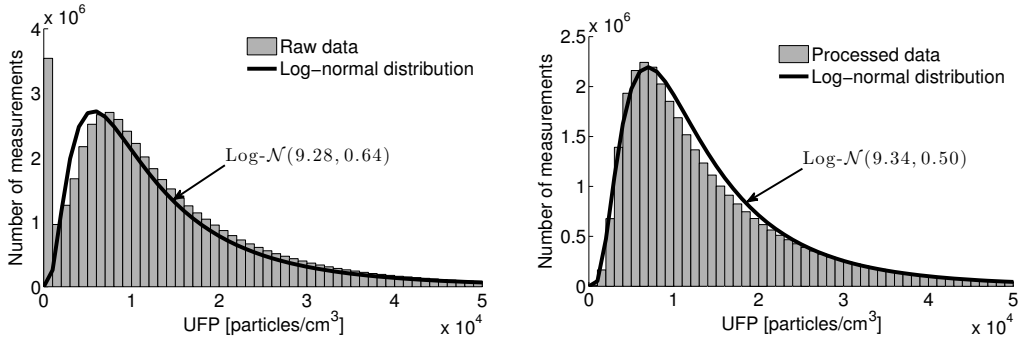

(a) Raw data.

(b) Processed data.

Figure 6: The log-normal distribution (black) with mean and standard deviation of the UFP data (gray). After calibration and filtering (processed data), the log-normal distribution accurately fits the distribution of the measurements.

Among others, the devices have to endure mobility, constant vibrations, high temperature and humidity variations, and long, unattended operating times.

Thus, we propose a three-fold validation approach to assess the quality of our measurements. We *(i)* analyze the statistical distribution of the monitored particle concentrations, *(ii)* evaluate the baseline signal of each device, and *(iii)* compare our measurements to data from two high-quality stations collected during the same time period but at different locations in Switzerland.

3.1. Statistical Distribution

The statistical distribution of data from many different scientific disciplines, including the concentration of ambient air pollutants, closely follows a log-normal distribution, *i.e.*, the logarithm of the measurements is normally distributed [21]. Previous work indicates that also UFPs are approximately log-normally distributed [22]. Here, we confirm that UFPs are log-normally distributed in urban environments. We show in Fig. 6 the distribution of the raw and processed (*i.e.*, applied calibration and filtering) data and the log-normal distributions with mean and standard deviation of the raw and processed data, respectively. Raw data are not log-normally distributed, as apparent from Fig. 6(a). However, as we show in Fig. 6(b), the distribution of the processed data nicely fits the log-normal distribution Log-$\mathcal{N}(\mu, \sigma^2)$ with $\mu = 9.34$ and $\sigma^2 = 0.50$.

3.2. Baseline Signal

We examine the correct offset of the MiniDiSCs, by looking at their baseline signals, *i.e.*, low-pass filtered measurements. We expect a similar baseline signal across all devices, because all devices take measurements in the same region (streetcars are not bounded to specific lines). We construct the baseline signal of each device by using a low-pass filter. We take for every 90 min time interval, the average time for a streetcar to cross the city twice, the 20th percentile of the measured concentrations. Our analysis confirms that during the two years analyzed the baseline signals are similar across all ten devices.

3.3. Comparison to High-Quality Data Sets

We compare our data set to UFP concentrations measured by fixed stations of the Swiss National Air Pollution Monitoring Network (NABEL). Five out of 16 NABEL stations are equipped

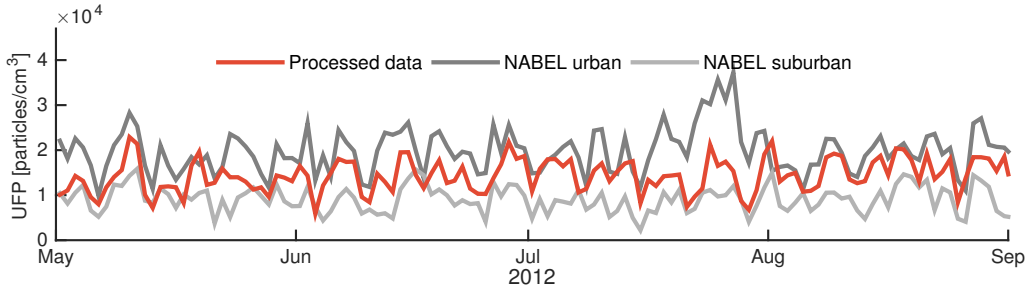

Figure 7: Daily average UFP concentration measured by the mobile sensor nodes in Zurich corresponds well to measurements of two fixed NABEL stations at urban (Pearson r = 0.49) and suburban (r = 0.55) locations.

with accurate UFP counters (condensation particle counters, CPCs). The stations are located in urban, suburban, and rural environments. For the comparison, we choose data from the stations with urban heavy traffic (Bern–Bollwerk) and suburban (Basel–Binningen) backgrounds, as these locations best reflect the topographical extremes of our measurement region in Zurich.

We compare the daily measured average particle concentrations from all mobile sensor nodes to daily averages measured by the two fixed stations. Thereof we depict in Fig. 7 a segment of four months. It shows that the three data sets have a similar trend, further reflected by the good Pearson correlations of r = 0.49 and r = 0.55 between our processed data and the urban and suburban located stations, respectively. The two NABEL data sets have a slightly lower correlation of r = 0.46. Furthermore, as we would expect, the daily average UFP concentration in Zurich ranges between the daily averages measured at the urban location with heavy traffic and at the suburban location.

The above results, namely the correct statistical distribution, the matching of all devices' baseline signals, and the good correlation and expected range of our data in comparison with the NABEL measurements, indicate a good quality of the processed data. In the following, we use this data set to derive land-use regression models for accurate high-resolution pollution maps.

4. Developing Land-Use Regression Models to Create High-Resolution Pollution Maps

Land-use regression (LUR) models are widely used to assess spatial variation of air pollutants, typically at an intraurban scale [23, 10]. LUR models use land-use and traffic characteristics (explanatory variables) to predict pollution levels for locations not covered by measurement devices. The general concept is based on two steps:

1. At all measurement locations the dependencies between explanatory variables (*e.g.*, population density, traffic volume, and terrain elevation) and monitored pollution levels are evaluated using linear regression.
2. The relationships found between concentrations monitored and the explanatory variables are used to predict concentration levels at locations without measurements but with available land-use data.

There are different approaches to construct LUR models. We use Generalized Additive Models (GAMs) [24], because they support non-linear relationships between monitored concentration levels and explanatory variables. Furthermore, GAMs have been used recently to analyze and model the spatio-temporal variability of particulate matter [25, 26].

Table 2: 12 explanatory variables are examined to build the air quality models for UFP pollution maps.

Variable [unit]	Variable [unit]
Population [inhabitants/ha]	Industry [industry buildings/ha]
Building height [floor levels/ha]	Heating [oil and gas heatings/ha]
Terrain elevation [average m/ha]	Road type [busiest road type/ha]*
Distance to next road [m]	Distance to next large road [m]†
Terrain slope [average degree/ha]	Terrain aspect [average degree/ha]
Traffic volume [vehicles per day/ha]	Distance to next traffic signal [m]

*Five road types: residential, tertiary, secondary, primary, and freeway.

†Road types classified as large: secondary, primary, and freeway.

4.1. Generalized Additive Models

We divide our data into different time periods and build for each time period a separate model. This yields 989 models with yearly, seasonal, monthly, biweekly, weekly, daily, and semi-daily (midnight–noon and noon–midnight) temporal resolutions. For all models we use the following relationship between pollution concentration and explanatory variables:

$$\ln(c_{\mathrm{num}}) = a + s_1(A_1) + s_2(A_2) + \cdots + s_n(A_n) + \epsilon, \tag{1}$$

where c_{num} denotes the UFP concentration, a the intercept, $s_1(A_1) \ldots s_n(A_n)$ the smooth functions $s_1 \ldots s_n$ with explanatory variables $A_1 \ldots A_n$, and ϵ the error term. The non-parametric functions $s_1 \ldots s_n$ are smooth regression splines. Through empirical evaluations we found that splines with an upper limit of three on the degrees of freedom and the logarithmic link function, $\ln(c_{\mathrm{num}})$ in (1), yields the best model residuals, which are the differences between measured and predicted values.

4.2. Selecting Explanatory Variables

We examine a set of 12 explanatory variables (listed in Table 2), which are typically used to derive LUR models [10]. Data to calculate population and industry densities, building heights, heating type, and elevation, slope, and aspect of the terrain are from the Swiss Federal Statistical Office. Road types and distances to next road and traffic signal are extracted from OpenStreetMap data. Average daily traffic volumes are obtained from the Department of Waste, Water, Energy, and Air of the Canton Zurich. Some of the data sets are based on measurements from 2007–2010. We assume that these explanatory variables did not change considerably compared to 2012–2014, which is the monitored and modeled time period. Most explanatory variables have a 100 m x 100 m (1 ha) resolution, which we use for all explanatory variables, as indicated in Table 2. This automatically sets the spatial resolution of the generated pollution maps.

It is crucial to examine the correlation between each pair of explanatory variables. Removing variables that have high correlation with each other helps to better distinguish individual contributions of different variables to the modeled particle concentration and prevents redundancy in the model [27]. We do not use population density and number of gas and oil heating households as both have a strong linear relationship with each other and with the number of floor levels (R^2 is larger than 0.6 [25]). Using the distance to the next traffic signal did not improve any of the tested models, and is, therefore, also removed from the modeling process.

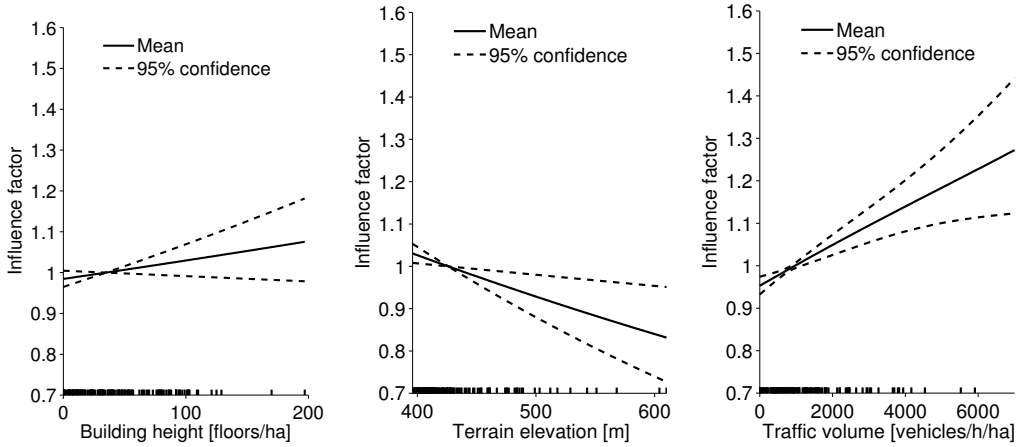

(a) Building height. (b) Elevation. (c) Traffic volume.

Figure 8: Typical influence factors. Building height and traffic volume have a positive while terrain elevation has a negative impact on UFP concentrations.

The terms on the right side in (1) have a multiplicative relationship with the particle concentration c_{num}, *i.e.*, $c_{\mathrm{num}} = e^{a} \cdot e^{s_1(A_1)} \cdot e^{s_2(A_2)} \cdots$. Thus, we can specify the influence of each explanatory variable A_n as a multiplicative influence factor $e^{s_n(A_n)}$. Fig. 8 depicts typical influence factors observed in our models. Building height and daily traffic volume have an amplifying while terrain elevation has a reducing impact on the particle concentration. The rugs on the x-axis show that a reduced number of measurements is available at the extremes resulting in decreased confidence bands.

4.3. UFP Data Aggregation

According to the resolution of the explanatory variables, the measured UFP concentrations of two years (April 2012 to March 2014) are projected on a grid with 13,200 cells, each of size $100\,\mathrm{m} \times 100\,\mathrm{m}$, covering the complete region of interest depicted in Fig. 5. The subset of the data used depends on the desired temporal resolution of the model, *i.e.*, for daily maps we consider measurements from a single day while for seasonal maps those from the entire season. For each grid cell i, we fetch the n_i measurements located in the cell to calculate the mean pollution concentration c_i^{m}. The applied GPS filter ensures that the localization is precise enough to correctly assign the measurements to their cells with high probability.

The measurements are (unevenly) distributed among 300–1300 different cells depending on the analyzed temporal subset of the data. For example, every black dot in Fig. 5 denotes a cell with at least 50 measurements when projecting the full two-year data set onto the grid. As model input we use the 200 cells with the highest number of measurements, which are mainly cells containing a streetcar stop. This ensures that the calculated means c_i^{m} are reliable and provides a good trade-off between spatial input distribution and model performance, as we will show in Sec. 5. Introducing prior weights on the cells (*e.g.*, using number of measurements per cell) does not improve the models.

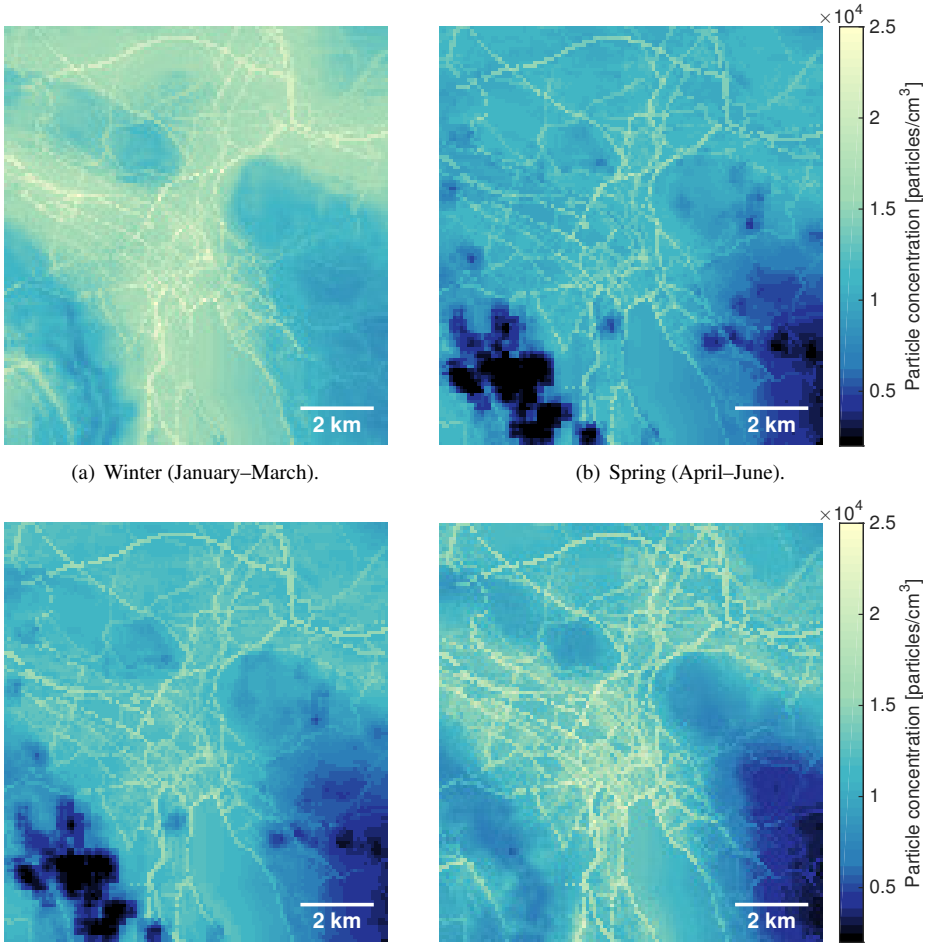

(a) Winter (January–March).

(b) Spring (April–June).

(c) Summer (July–September).

(d) Fall (October–December).

Figure 9: Seasonal UFP pollution maps with a spatial resolution of 100 m × 100 m for Zurich (Switzerland).

4.4. Model Output: High-Resolution Pollution Maps

We use the method described above to develop models for pollution maps with different temporal resolutions. For instance, the output of the models with seasonal resolution (winter, spring, summer, and fall) is shown in Fig. 9. In general, terrain elevation, building heights, and traffic density have the highest influence on the predicted pollution levels. Further, we see that the pollution levels are higher in winter and fall than in spring and summer. This is due to frequent high-inversion fog (fog above the surface, which does not completely dissipate) in Zurich from October to March preventing the pollutants to be lifted from the surface and therewith increasing pollution concentration near the ground [28]. The topographical structure around Zurich makes the city prone to inversion fog as it is closely surrounded by hills in the north-east and south-west.

5. Revealing the Temporal Resolution Limit

This section evaluates the performance of the 989 generated air quality models with yearly to semi-daily temporal resolutions based on our measurements from April 2012 to March 2013 (including eight weeks of maintenance work without measurements). These are 1 yearly, 4 seasonal, 11 monthly, 23 biweekly, 44 weekly, 309 daily, and 597 semi-daily models.[2] Our evaluation reveals the following findings:

- Models for pollution maps with yearly to weekly time scales have an accuracy that is comparable to recently published state-of-the-art air quality models.
- Pollution maps with daily and semi-daily temporal resolutions are less accurate due to the reduced number of measurements available to derive the models.

5.1. Metrics and Evaluation Methodology

We use three standard metrics to evaluate our models [29].

Factor of 2 measure (FAC2): Quantitatively analyzes scatter plots (predicted concentrations plotted against measured concentrations) by evaluating the fraction of data points that lie inside the factor two area, *i.e.*, fraction of data that satisfy:

$$0.5 \leq \frac{c_i^{\mathrm{p}}}{c_i^{\mathrm{m}}} \leq 2.0, \tag{2}$$

where c_i^{p} is the model predicted and c_i^{m} is the average measured concentration of grid cell i. This measure is based on the assumption that an accurate model for pollution maps should have a relative scatter less than a factor of two [29].

Root-mean-square error (RMSE): Quantifies the difference between the predicted and measured particle concentrations:

$$\mathrm{RMSE} = \Big(\frac{\sum_{i=1}^{N} \left(c_i^{\mathrm{p}} - c_i^{\mathrm{m}}\right)^2}{N} \Big)^{0.5}, \tag{3}$$

where N denotes the number of cells used in the evaluation.

Adjusted coefficient of determination (R^2): Indicates from 0 to 1 how well the predictions fit the measurements (R^2 = 1 denotes a perfect fit). R^2 reflects the linear relationship between predicted and measured values, hence, it is insensitive to additive and multiplicative errors.

For all evaluations we perform a 10-fold cross-validation. That is, we randomly remove 10 % of the measurements and create (calibrate) the model using the remaining 90 % of the data. We use the predictions at the locations of the removed 10 % to evaluate the metrics above. We repeat this procedure 40 times to have a good coverage of the complete data set.

5.2. Model Performance

We first ensure that the models have no systematic bias and then use the metrics above to evaluate their accuracy.

Trustworthy models should not have any systematic bias in their predictions. In general, the predictions did not show any bias. We show this exemplary in Fig. 10 on scatter plots of seasonal pollution maps (see Fig. 9). The dashed lines denote the factor of two area, *i.e.*, slopes of 0.5 and 2, and the optimal 1-to-1 relation, *i.e.*, slope of 1. The linear regression lines (solid) are very close to the 1-to-1 lines for all depicted seasons, indicating the absence of systematic errors.

[2] For some days we do not have two semi-daily models because the nodes were in operation only for part of the day.

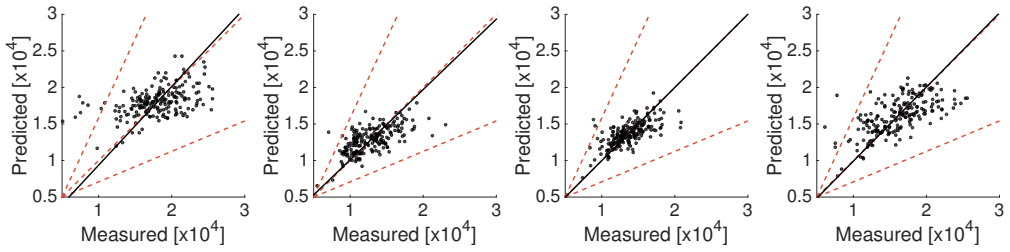

(a) Winter. (b) Spring. (c) Summer. (d) Fall.

Figure 10: Scatter plots. Model predicted versus measured UFP concentrations (particles/cm^3) for seasonal pollution maps. The dashed lines depict the factor of two area (slopes of 0.5 and 2) and the 1-to-1 relation (slope of 1). All linear regression lines (solid) are very close to the 1-to-1 lines.

Fig. 11 shows the three metrics as box plots for all analyzed temporal time scales. The central mark of each box plot denotes the median, edges show the 25th and 75th percentiles, whiskers cover the most extreme data points without outliers, and the crosses depict the outliers. Models with yearly to weekly temporal resolutions have very high FAC2s, while daily and semi-daily predictions have a considerable number of models with lower FAC2 values, *i.e.*, many predictions are more than a factor of two off. The RMSEs grow with increasing temporal resolution. Yearly to weekly pollution maps have low RMSEs, which are in range of recently published air quality models [10]. Models with higher temporal resolutions, such as daily and semi-daily pollution maps, have on average 38 % higher RMSEs.

The average R^2 of yearly to monthly maps is 0.38, and slightly decreases for shorter time scales. Recently published air quality models for particulate matter have R^2 values in 0.17–0.82 [10]. Most of these models are based on installations that are just in place for a short time (*i.e.*, days or weeks) with measurement devices employed at a carefully selected set of around 40 locations, on average. In our deployment we have a large number of measurement locations, but (perhaps counterintuitively) with many locations it is more difficult to get predictions with high R^2 values [30, 31]. We found that a restriction to 200 grid cells leads to a good trade-off among the considered metrics, as exemplified in Fig. 12 for yearly pollution maps. Models created with a small number of grid cells have good R^2s but their validity at locations not covered by the input cells is limited, which results in poor FAC2 and RMSE values. Models developed with many grid cells (> 300) have poor R^2s and RMSEs. Among others, this is because the number of cells with unreliable average cell concentrations increases as the calculated means are more and more based on a limited number of measurements (remember that the cells are favored according to the number of measurements per cell).

5.3. Challenges of Developing Temporal High-Resolution Maps

We observe on all performance metrics examined that for higher temporal resolutions it is more difficult to derive accurate pollution maps. The main problem is the reduced number of measurements available to calculate the mean particle concentration per cell, leading to the following complications:

- The calculated mean of a grid cell is less reliable as it is based on a smaller number of measurements.

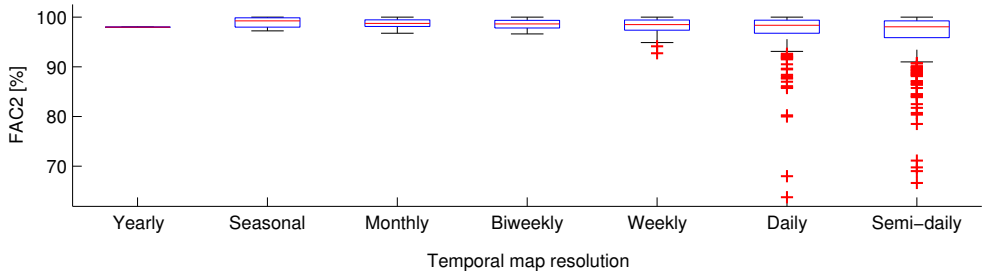

(a) Factor of 2 statistic (FAC2).

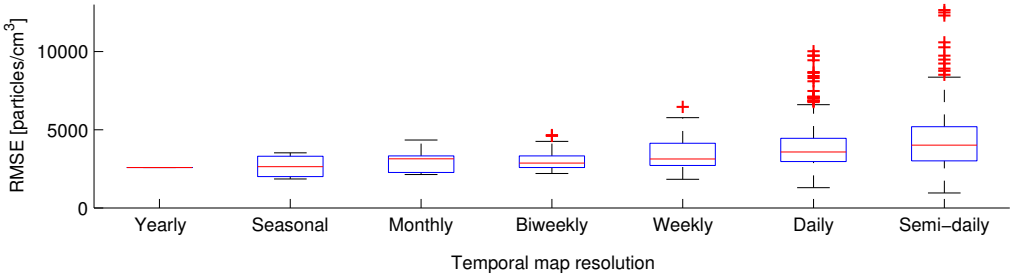

(b) Root-mean-square error (RMSE).

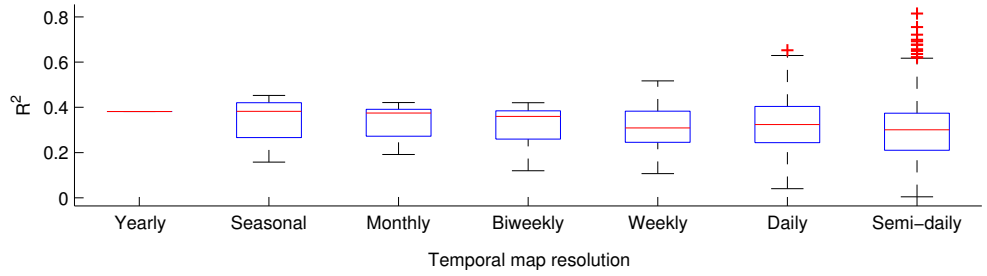

(c) Adjusted coefficient of determination (R^2).

Figure 11: Models with yearly to weekly temporal resolutions have a good quality with high FAC2 values, low RMSEs, and acceptable R^2 coefficients. Models with higher temporal resolutions perform less well.

- Erroneous and inaccurate measurements (*e.g.*, due to outliers, sensor noise, and outdated calibration) have a higher impact on the mean value of a cell.

To quantitatively support our claims, we examine the relative standard error (RSE) of each cell, which is a good indicator of the reliability of a cell's mean:

$$\mathrm{RSE_i} = \frac{\sigma_i^{\mathrm{m}}}{\sqrt{n_i} \cdot c_i^{\mathrm{m}}} \cdot 100, \tag{4}$$

where σ_i^{m} is the standard deviation of the n_i measurements of cell i. Fig. 13(a) illustrates how the average RSE declines with increasing number of measurements per cell. Models derived from

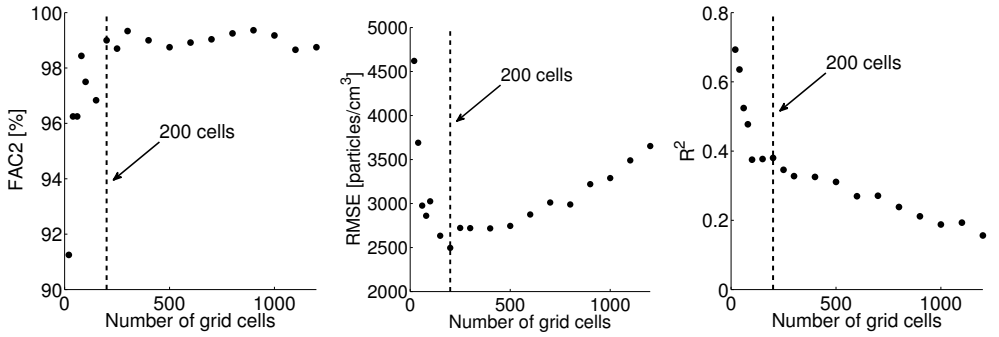

(a) FAC2. (b) RMSE. (c) R^2.

Figure 12: Yearly pollution maps modeled with 20–1200 grid cells. The models achieve a good performance trade-off with 200 cells (dashed line).

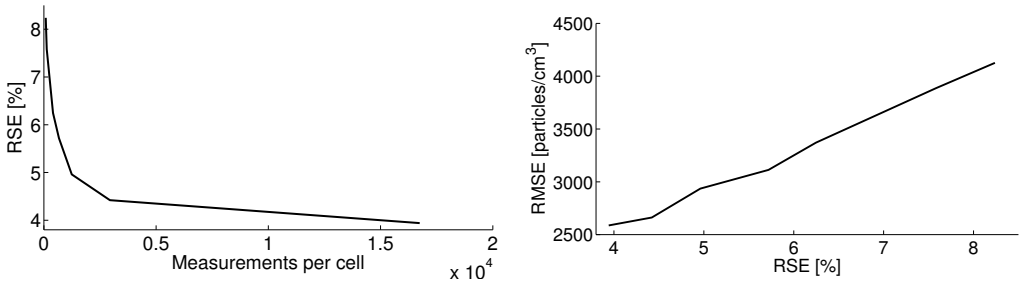

(a) RSE of the cells depending on the number of measurements per cell.

(b) RMSE of the pollution maps depending on the RSE of the cells.

Figure 13: With increased number of measurements the relative standard error (RSE) of the cells' mean decreases. Models based on cells with small RSEs have low RMSEs.

cells with small RSEs have lower RMSEs, as shown in Fig. 13(b). The RSE increase from 4 % to 8 % results in a 60 % rise of the models' RMSEs. Note that we verified that using the median instead of the mean of a cell does not yield improved model performance.

In the following, we propose a new modeling approach to increase the number of measurements per cell and, therewith, improve the accuracy of models with high temporal resolution.

6. Increasing the Temporal Resolution Limit

We propose a novel modeling approach, which is able to make use of past pollution measurements to increase the accuracy of highly temporally resolved pollution maps. For that, we introduce a history database containing our measurements from the last 12 months annotated with metadata describing the environmental conditions at time of measurement. We exploit that concentrations of air pollutants show a high correlation with various environmental conditions (*e.g.*, temperature) and the current weekday [26, 32, 33]. The data selector depicted in Fig. 14, selects from the history database those measurements that were performed on the same weekday

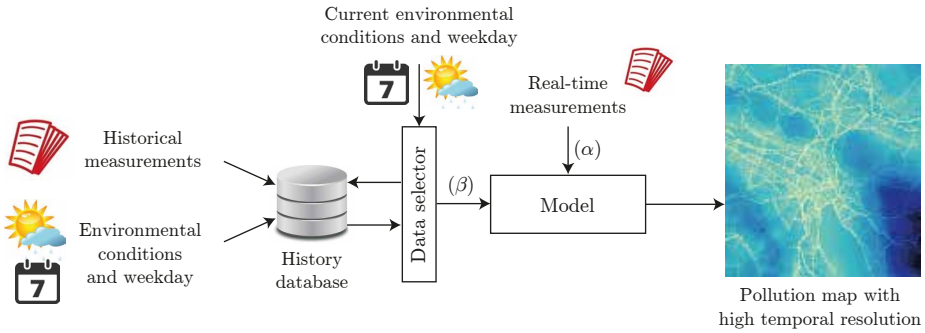

Figure 14: Additional data (β) from a database with historical measurements is used to enhance the original data set (α) to derive pollution maps with high temporal resolutions. The data selector ensures that only historical measurements are used, which were measured under similar environmental conditions as the average condition of the modeled time period.

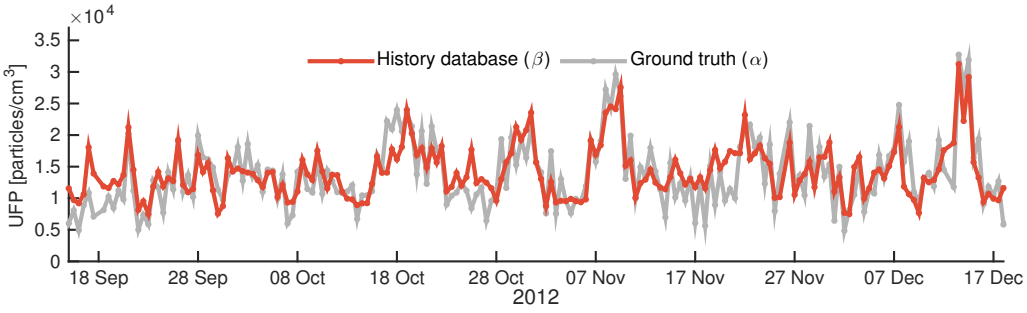

Figure 15: Average semi-daily concentrations based on the history database closely matches ground truth data measured on these days (Pearson r = 0.74).

and under similar environmental conditions as the average condition of the modeled time period. These historical measurements (β) are used together with measurements from the modeled time period (α) to calculate temporally resolved pollution maps, as shown in Fig. 14. For example, assume we want to create a pollution map for a sunny but windy Saturday. We enrich the original measurements (α) from that Saturday with historical measurements (β) gathered on a past sunny, windy Saturday and use both data sets to compute an accurate pollution map.

In the following, we show the feasibility of this novel approach on the case study of semi-daily pollution maps, where the standard model did not deliver a satisfactory accuracy.

6.1. Data Annotation

We feed the history database with 15 million UFP measurements from a complete year (April 2012 to March 2013). We annotate the measurements with the environmental conditions measured in the city center during this time period by a high-quality governmental station (the triangle in Fig. 5 denotes the location of the station). The station provides 30 min averages of a diverse set of environmental variables, namely humidity, atmospheric pressure, radiation, precipitation, temperature, wind direction, wind speed, and nitrogen oxide (NO_x) concentration.

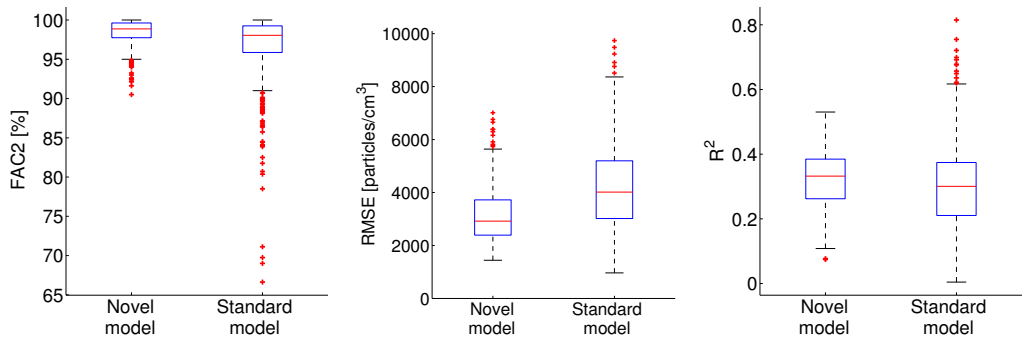

(a) FAC2. (b) RMSE. (c) R^2.

Figure 16: The novel method with a history database helps to increase the quality of semi-daily pollution maps. On average, the RMSE is 26 % lower using the novel model compared to the standard model.

6.2. Data Selector and Quality of Selected Data

The data selector, depicted in Fig. 14, fetches based on the average environmental condition of the modeled half-day those measurements from the history database, which are most likely to be similar to the real measurements from that half-day. To find the best data selector, we evaluate all possible combinations of environmental variables. We introduce a deviation parameter, which controls how closely the metadata of the fetched measurements has to match the given conditions. For example, allowing 20 % deviation and a temperature of 15 °C, the data selector returns all data measured at 15 °C $\pm$ 20 %, whereas 100 % refers to the maximum range in the database.

We evaluate the best data selector by comparing for a complete year the average semi-daily UFP concentration supplied by the two input data sets (β) and (α) depicted in Fig. 14. We observe that the fetched data from the history database (β) are closest to the actual measured concentrations (α) if the selection is based on the following three criteria: temperature, wind direction, and NO_x concentration with an allowed deviation of 10 %. The two data sets have a high Pearson correlation of 0.74 and a low average absolute difference of 2,500 particles/cm^3, as shown on a three-month extract in Fig. 15. In this way, we attain on average a 14x increase in data volume from 19,000 (α) to 260,000 (α+β) measurements per half-day.

6.3. Increased Quality of Semi-Daily Pollution Maps

The extended number of measurements helps to derive pollution maps with a higher accuracy. We compare our modeling approach with the standard approach using the three performance metrics. Fig. 16 shows that using our novel modeling approach increases FAC2s by 2 %, R^2s by 6 %, and decreases RMSEs by 26 %, on average. The semi-daily pollution maps created with the new models achieve a similar accuracy as the weekly pollution maps created with the standard models.

This new modeling approach advances the generation of accurate pollution maps with high temporal resolutions and simultaneously enables the forecasting of pollution maps for specific environmental conditions, *e.g.*, by using weather forecast data to create pollution maps for the next hours or days.

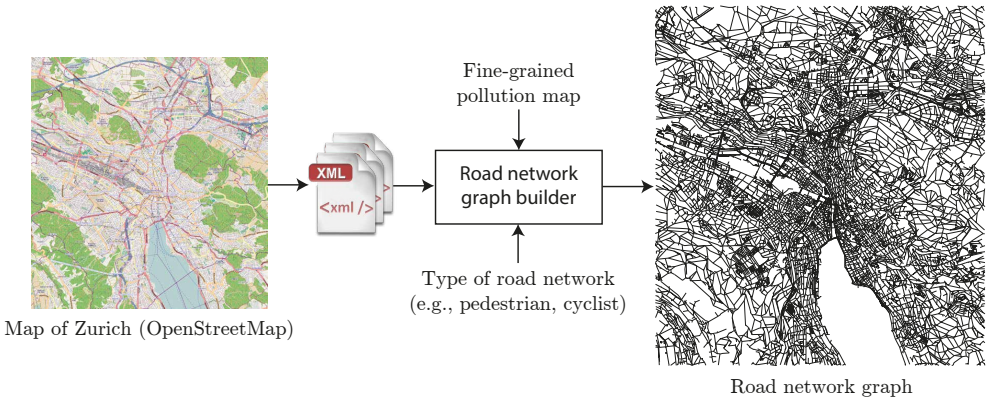

Figure 17: The road network builder uses OpenStreetMap data to create different types of road network graphs, where nodes represent street crossroads and dead-end streets and edges connect two consecutive nodes. Each edge has two corresponding weights representing the distance and pollution exposure between the two connected nodes, respectively.

7. Application Example

Many companies offer route planning services (*e.g.*, GoogleMaps [34], MapQuest [35], and TomTom [36]), which evaluate the best route between origin and destination based on different criteria, such as distance, journey time, and least total fuel consumption for various transportation modes. However, the general public, especially pedestrian and cyclist commuters, are increasingly concerned about the adverse health effects of urban air pollution and, hence, wish to minimize their exposure to airborne pollutants [37]. Up to today, the lack of spatial resolved pollution data hinders route planners to provide such air pollution related services.

We use the generated high-resolution air quality models to derive a novel cost function for all street segments of Zurich's road network. The cost function expresses the expected UFP exposure when traversing the respective street segment. We implement this new cost function in a route finding algorithm to compute health-optimal routes and compare them to the traditionally used shortest path. Therewith, we analyze the potential of reducing the number of inhaled particles while roaming the city. Finally, we implement the application in iOS for iPhones and iPads and make it available for free on the App Store as *hRouting–The Health-Optimal Route Planner*.[3]

7.1. Road Network Graph

We use data from OpenStreetMap to construct a graph of Zurich's road network.We export the area of Zurich in the OSM XML file format, which then is processed by our road network graph builder to compute a graph of Zurich's road network, as depicted in Fig. 17. Depending on which type of road network is requested (*e.g.*, for pedestrians, cyclists, or car drivers), a different graph is generated.

We represent the road network by an undirected graph $G = (V, E, W_d, W_p)$ comprising a set V of vertices (nodes), a set E of edges each connecting a pair of nodes, and two sets of edge weights W_d and W_p. Each node $v_i \in V$ represents a crossroad or a dead-end street of the road network. There is an edge $e_j \in E$ between two nodes of V if the nodes are directly connected by

[3] `https://itunes.apple.com/us/app/hrouting-health-optimal-route/id931299863`

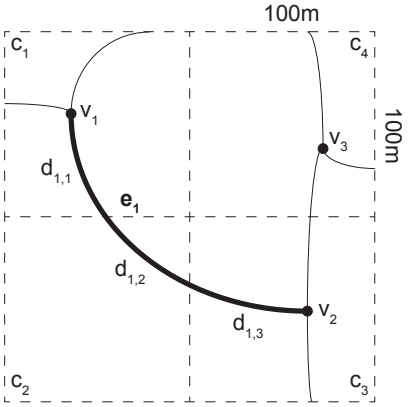

Figure 18: Road segment e_1 connecting the two nodes v_1 and v_2 penetrates three 100 m x 100m grid cells with a corresponding pollution exposure of c_1, c_2, and c_3.

a road segment (*i.e.*, without a crossroad in between). Each edge is associated with two weights. Weight $w_{d,j} \in W_d$ denotes the length of the road segment between the pair of nodes connected by edge e_j. Weight $w_{p,j} \in W_p$ denotes the expected pollution exposure on the road segment represented by edge e_j. We assume that the travel time between two nodes of an edge $e_j \in E$ is proportional to the distance $w_{d,j}$. The number of particles a human inhales is proportional to the time of exposure [38]. Hence, we multiply the modeled particle concentration along edge e_j with the length of the corresponding road segment:

$$w_{p,j} = \sum_{k=1}^{n} d_{j,k} \cdot c_k, \tag{5}$$

where n is the number of 100 m x 100 m grid cells the edge penetrates, $d_{j,k}$ is the length of edge e_j penetrating grid cell k, and c_k is the modeled pollution concentration in grid cell k. Note that the sum of the n subsegments is equal to the total length of the road segment, *i.e.*, $w_{d,j} = \sum_{k=1}^{n} d_{j,k}$.

We illustrate the above weight functions on a simple example depicted in Fig. 18. The two crossroads v_1 and v_2 are connected by road segment e_1, which cuts through three grid cells with modeled pollution concentrations c_1, c_2, and c_3. We calculate the weights $w_{d,1}$ and $w_{p,1}$ as:

$$w_{d,1} = d_{1,1} + d_{1,2} + d_{1,3}, \tag{6}$$

$$w_{p,1} = d_{1,1} \cdot c_1 + d_{1,2} \cdot c_2 + d_{1,3} \cdot c_3. \tag{7}$$

7.2. Finding the Least-Cost Path

We use all road segments available (including those only accessible by pedestrians) to create graph G representing the road network of Zurich consisting of $|V| = 27,000$ nodes (*i.e.*, crossroads and dead-end streets) and $|E| = 74,000$ edges. We implement the widely used A* pathfinding algorithm [39] to find the least-cost path between two nodes of the road network with respect to the two introduced weight metrics. A* requires for every node $v_i \in V$ a heuristic estimate $h(v_i)$ of the cost involved to reach from node v_i the destination node. A* only guaranties optimality of the computed path, if an admissible heuristic is used, *i.e.*, if the heuristic

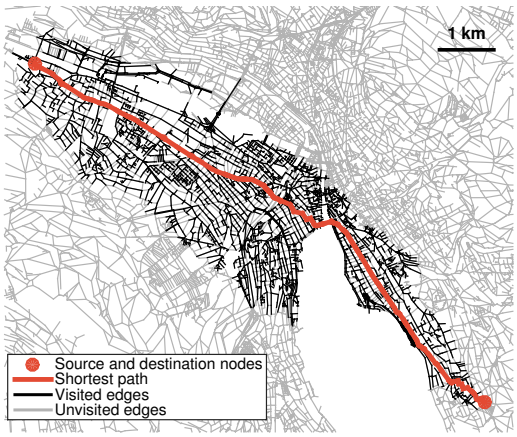

Figure 19: The A* pathfinding algorithm makes use of a heuristic estimation of the cost involved to reach the destination node enabling a goal-directed exploration of the road network graph.

never overestimates the cost of reaching the destination node. To ensure optimality, we use line-of-sight distance as heuristic when computing the shortest path. To compute the health-optimal path (with respect to UFP exposure), we use the product of line-of-sight distance and minimal pollution concentration within the modeled area. With the help of these admissible heuristics, A* is able to perform a goal-directed exploration and quickly find the least-cost path, as illustrated in Fig. 19 for the shortest path between a pair of source-destination nodes.

7.3. Comparing Shortest and Health-Optimal Paths

In the following, we study how much urban dwellers can reduce their pollution exposure by not taking the shortest but the health-optimal path between two random locations in the city. We randomly pick from the road network graph 1000 source-destination pairs. We require a minimum line-of-sight distance of 5 km between source and destination nodes to prevent very short paths where with high probability the shortest and health-optimal paths are identical. For these 1000 source-destination pairs we compute for both introduced edge weights the least-cost paths using the A* pathfinding algorithm. Then, we compare the length and the pollution exposure of the two routes. To evaluate the pollution exposure, we use the seasonal UFP model depicted in Fig. 9(d), which is based on our pollution measurements from October to December 2012.

We find that taking the health-optimal path instead of the shortest path yields an exposure reduction of 7.1 % ($6.8 \cdot 10^6$ particles/cm^3·m) on average. This comes at a price of longer travel distances, the length of the health-optimal path is 6.4 % (548 m) longer on average. However, the difference between the shortest and health-optimal paths largely depend on the given source and destination nodes, as illustrated in Fig. 20. The computed routes are completely different in Fig. 20(a), partly overlap in Fig. 20(b), and are almost identical in Fig. 20(c). The additional distance (and hence exposure time) incurred by not following the shortest path only pays off if significantly less polluted road segments are available nearby. We can clearly observe this in the depicted health-optimal paths in Fig. 20, which if possible pass through or are close to public green spaces characterizing areas with low pollution concentrations.

The achievable reduction also highly depends on the specific distribution of the air pollutants. We reuse the 1000 source-destination pairs from above to compare the shortest paths with the

(a) Albisrieden to Wollishofen. (b) Wiedikon to Witikon. (c) Hönggerberg to ETH Zentrum.

Figure 20: Three exemplary source-destination pairs within the city of Zurich, Switzerland. In (a) the shortest and health-optimal routes are completely different while they partly overlap in (b) and (c).

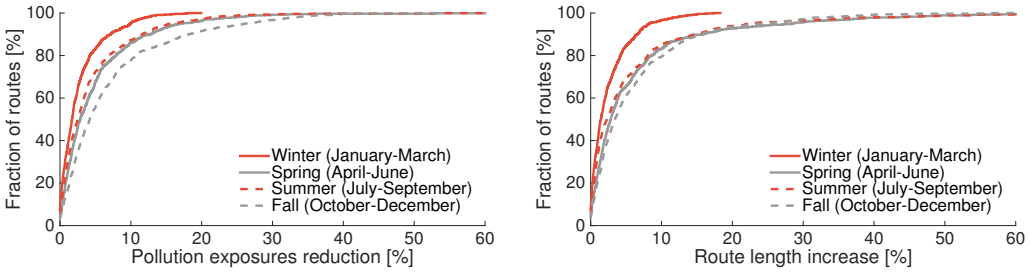

(a) Reduction in pollution exposure. (b) Increase in route length.

Figure 21: The health-optimal paths minimize the expected exposure to UFPs while being only slightly longer than the shortest paths. The differences between the health-optimal and shortest paths are most significant in the fall months.

health-optimal paths for all four seasonal air quality models depicted in Fig. 9. We find that during the fall months the reduction in pollution exposure is more significant than during the winter months, as depicted on the CDF plots in Fig. 21. This is because during the fall months the pollution concentration along major roads is considerably higher than on smaller streets close by, as observable in Fig. 9(d). In contrast, during winter months this pollution gradient is smaller.

8. Related Work

Monitoring airborne pollutants with mobile, low-cost sensors has gained much attention in recent years. Low-cost gas sensors are often embedded in custom-built, personal sensor nodes that are part of participatory sensing networks [40, 41]. Participants can directly monitor the exposure level at locations where they spent their time [42]. However, reaching the critical mass of users to get a coherent picture of the exposure situation in the area of interest is a formidable challenge and may require hundreds to thousands of contributors. Our approach

uses a small number of non-personal sensor nodes deployed on top of public transport vehicles to automatically obtain a constant coverage in the area of interest.

There are different kinds of models that can be developed to predict intraurban pollution concentrations, such as proximity-based assessment, statistical interpolation, LUR, line dispersion models, and novel machine learning and data mining techniques [23, 33, 42]. In this work, we develop LUR models since they have, compared to other models, a relatively low computational overhead, which is beneficial when deriving many hundreds of models. Above all, in the past, LUR models were applied to predict the concentration of a wide range of air pollutants [10]. Most of these models are based on data from static monitoring stations installed at a small set of hand-picked locations (typically around 40) for some days or couple of weeks [10]. In contrast, our mobile sensor nodes cover a much larger number of locations, *i.e.*, every day around 300 grid cells of size 100 m x 100 m. Therewith, we develop maps with a high spatio-temporal resolution.

A number of studies address the challenge of developing models with high temporal resolutions. Liu et al. [26] derive daily $PM_{2.5}$ maps with a spatial resolution of 4 km by using satellite data in combination with meteorological features. Su et al. [30] extend their NO_2 and NO models with hourly meteorological conditions, such as wind speed and wind direction, to create pollution maps with an hourly resolution. However, it remains unclear how much the meteorological data helps to improve their models. Furthermore, the performance of the hourly resolved pollution maps was not evaluated.

Clifford et al. [32] and Mølgaard et al. [22] develop UFP models with high temporal resolutions by using not only traffic and land-use characteristics data but also meteorological variables as model covariates. Both works solely model temporal variability as their data originates from a single static station.

Many of the above works use meteorological data to enhance their models, *i.e.*, [26, 30, 32, 22]. However, their methods of integrating meteorological data into the modeling process only work if *(i)* the specific meteorological conditions are known at each measurement location and *(ii)* the meteorological conditions are significantly different among locations for a given instant in time. Most often, both conditions do not apply for spatially resolved intraurban data sets.

Several recent studies have analyzed how the choice of route impacts exposure to air pollutants. Hertel et al. [43] analyze the commute of 50 persons and find that a proper selection of route can significantly reduced the air pollution exposure. Due to the lack of spatially resolved air pollution data, diurnal traffic is used as a proxy for air pollution exposure. Sharker et al. [44] use data from sparsely distributed static measurement stations to estimate the pollution level of each street segment of the analyzed road network. The weight of a street segment is calculated as product of the estimated pollution level and expected travel time through the street segment. Finally, Allemann et al. [45] outline the health-atlas platform, a route planing service that plans to incorporate different modes of transportation, personal mobility restrictions, and air pollution measurements (governmental and crowd-sourced). This should enable the system to propose to its users the healthiest path between origin and destination.

9. Conclusions

Today, little is known about the spatial distribution of air pollutants in urban environments. We address this problem by deploying mobile sensor nodes on top of public transport vehicles in the city of Zurich, Switzerland. We take advantage of the transport network's coverage and regular schedule to collect one of the largest spatially resolved data set containing over 50 million ultrafine particle measurements. We develop land-use regression models to create pollution

maps with a high spatial resolution and study their temporal resolution limit. We reveal that the accuracy of pollution maps with sub-weekly temporal resolution suffers from the limited number of measurements available to model the pollution concentrations. We tackle this problem by proposing a novel modeling approach, which is able to make use of past measurements to increase the available data volume. Therewith, we develop accurate ultrafine particle pollution maps with a high spatio-temporal resolution. These maps are valuable to the general public as well as to environmental scientists and epidemiologists to shed more light on the adverse health effects of ultrafine particles. We believe that our findings promote the accurate, detailed, and timely assessment of air quality in urban environments.

Acknowledgements. We thank the anonymous reviewers for their valuable comments. Further, we thank Marco Zimmerling who provided valuable feedback on the initial version of this paper. This work was funded by NanoTera.ch with Swiss Confederation financing.

References

[1] D. Mage, G. Ozolins, P. Peterson, A. Webster, R. Orthofer, V. Vandeweerd, M. Gwynne, Urban air pollution in megacities of the world, Atmospheric Environment 30 (1996) 681–686.

[2] P. Penttinen, K. L. Timonen, P. Tiittanen, A. Mirme, J. Ruuskanen, J. Pekkanen, Number concentration and size of particles in urban air: effects on spirometric lung function in adult asthmatic subjects., Environmental Health Perspectives 109 (2001) 319–323.

[3] R. M. Harrison, J. Yin, Particulate matter in the atmosphere: which particle properties are important for its effects on health?, Science of The Total Environment 249 (2000) 85–101.

[4] G. Hoek, H. Boogaard, A. Knol, J. De Hartog, P. Slottje, J. G. Ayres, P. Borm, B. Brunekreef, K. Donaldson, F. Forastiere, et al., Concentration response functions for ultrafine particles and all-cause mortality and hospital admissions: results of a European expert panel elicitation, Environmental Science & Technology 44 (2009) 476–482.

[5] S. Devarakonda, P. Sevusu, H. Liu, R. Liu, L. Iftode, B. Nath, Real-time air quality monitoring through mobile sensing in metropolitan areas, in: Proceedings of the 2nd Workshop on Urban Computing (UrbComp), ACM, 2013.

[6] G. L. Re, D. Peri, S. D. Vassallo, Urban air quality monitoring using vehicular sensor networks, Advances onto the Internet of Things 260 (2014) 311–323.

[7] O. Saukh, D. Hasenfratz, C. Walser, L. Thiele, On rendezvous in mobile sensing networks, in: Real-World Wireless Sensor Networks (RealWSN), Springer, 2014, pp. 29–42.

[8] D. Hasenfratz, O. Saukh, C. Walser, C. Hueglin, M. Fierz, L. Thiele, Pushing the spatio-temporal resolution limit of urban air pollution maps, in: Proceedings of the 12th International Conference on Pervasive Computing and Communications (PerCom), IEEE, 2014, pp. 69–77.

[9] M. Fierz, C. Houle, P. Steigmeier, H. Burtscher, Design, calibration, and field performance of a miniature diffusion size classifier, Aerosol Science and Technology 45 (2011) 1–10.

[10] G. Hoek, R. Beelen, K. de Hoogh, D. Vienneau, J. Gulliver, P. Fischer, D. Briggs, A review of land-use regression models to assess spatial variation of outdoor air pollution, Atmospheric Environment 42 (2008) 7561–7578.

[11] J. J. Li, B. Faltings, O. Saukh, D. Hasenfratz, J. Beutel, Sensing the air we breathe–the OpenSense Zurich dataset, in: Proceedings of the 26th International Conference on Artificial Intelligence (AAAI), 2012.

[12] K. Aberer, M. Hauswirth, A. Salehi, A middleware for fast and flexible sensor network deployment, in: Proceedings of the 32nd International Conference on Very Large Data Bases (VLDB), 2006, pp. 1199–1202.

[13] M. Keller, J. Beutel, O. Saukh, L. Thiele, Visualizing large sensor network data sets in space and time with vizzly, in: Proceedings of the 7th International Workshop on Practical Issues in Building Sensor Network Applications (SenseApp), IEEE, 2012, pp. 925–933.

[14] B. Buchli, M. Yuecel, R. Lim, T. Gsell, J. Beutel, Demo abstract: Feature-rich platform for WSN design space exploration, in: Proceedings of the 10th International Conference on Information Processing in Sensor Networks (IPSN), ACM/IEEE, 2011, pp. 115–116.

[15] SGX Sensortech, MiCS-OZ-47 ozone sensor (datasheet), `http://sgx.cdistore.com/datasheets/e2v/a1a-mics-oz-47_1_s1%20081231.pdf`, 2014.

[16] Alphasense, CO-B4 4-Electrode carbon monoxide sensor (datasheet), `http://www.alphasense.com/WEB1213/wp-content/uploads/2014/10/COB4.pdf`, 2014.

[17] Alphasense, NO2-B4 4-Electrode nitrogen dioxide sensor (datasheet), `http://www.alphasense.com/WEB1213/wp-content/uploads/2013/11/NO2B4.pdf`, 2014.

[18] D. Hasenfratz, S. Sturzenegger, O. Saukh, L. Thiele, Spatially resolved monitoring of radio-frequency electromagnetic fields, in: Proceedings of the 1st International Workshop on Sensing and Big Data Mining (SenseMine), ACM, 2013.
[19] Sensirion, SHT10 humidity and temperature sensor, http://www.sensirion.com/fileadmin/user_upload/customers/sensirion/Dokumente/Humidity/Sensirion_Humidity_SHT1x_Datasheet_V5.pdf, 2014.
[20] D. Hasenfratz, O. Saukh, L. Thiele, Model-driven accuracy bounds for noisy sensor readings, in: Proceedings of the 9th International Conference on Distributed Computing in Sensor Systems (DCOSS), IEEE, 2013, pp. 165–174.
[21] E. Limpert, W. A. Stahel, M. Abbt, Log-normal distributions across the sciences: Keys and clues, BioScience 51 (2001) 341–352.
[22] B. Mølgaard, T. Hussein, J. Corander, K. Hämeri, Forecasting size-fractionated particle number concentrations in the urban atmosphere, Atmospheric Environment 46 (2012) 155–163.
[23] M. Jerrett, A. Arain, P. Kanaroglou, B. Beckerman, D. Potoglou, T. Sahsuvaroglu, J. Morrison, C. Giovis, A review and evaluation of intraurban air pollution exposure models, Exposure Science and Environmental Epidemiology 15 (2005) 185–204.
[24] T. J. Hastie, R. J. Tibshirani, Generalized additive models, volume 43, Chapman & Hall/CRC, 1990.
[25] I. Barmpadimos, C. Hueglin, J. Keller, S. Henne, A. Prévôt, Influence of meteorology on PM_{10} trends and variability in Switzerland from 1991 to 2008, Atmospheric Chemistry and Physics 11 (2011) 1813–1835.
[26] Y. Liu, C. J. Paciorek, P. Koutrakis, Estimating regional spatial and temporal variability of $PM_{2.5}$ concentrations using satellite data, meteorology, and land use information, Environmental Health Perspectives 117 (2009) 886–892.
[27] L. Jackson, N. Carslaw, D. Carslaw, K. Emmerson, Modelling trends in OH radical concentrations using generalized additive models, Atmospheric Chemistry and Physics 9 (2009) 2021–2033.
[28] Federal Office for the Environment, Measurement results from the Swiss national air pollution monitoring network NABEL, 2009.
[29] J. Chang, S. Hanna, Air quality model performance evaluation, Meteorology and Atmospheric Physics 87 (2004) 167–196.
[30] J. G. Su, M. Brauer, B. Ainslie, D. Steyn, T. Larson, M. Buzzelli, An innovative land use regression model incorporating meteorology for exposure analysis, Science of the Total Environment 390 (2008) 520–529.
[31] X. Basagaña, M. Rivera, I. Aguilera, D. Agis, L. Bouso, R. Elosua, M. Foraster, A. de Nazelle, M. Nieuwenhuijsen, J. Vila, N. Kuenzli, Effect of the number of measurement sites on land use regression models in estimating local air pollution, Atmospheric Environment 54 (2012) 634–642.
[32] S. Clifford, S. Low C., T. Hussein, K. Mengersen, L. Morawska, Using the generalised additive model to model the particle number count of ultrafine particles, Atmospheric Environment 45 (2011) 5934–5945.
[33] Y. Zheng, F. Liu, H.-P. Hsie, U-Air: When urban air quality inference meets big data, in: Proceedings of the 19th International Conference on Knowledge Discovery and Data Mining (SIGKDD), ACM, 2013, pp. 1436–1444.
[34] GoogleMaps, Route planner, http://www.maps.google.com, 2014.
[35] MapQuest, Route planner, http://www.mapquest.com, 2014.
[36] TomTom, Route planner, http://www.routes.tomtom.com, 2014.
[37] J. J. De Hartog, H. Boogaard, H. Nijland, G. Hoek, Do the health benefits of cycling outweigh the risks?, Environmental health perspectives 118 (2010) 1109–1116.
[38] H. Kruize, O. Hänninen, O. Breugelmans, E. Lebret, M. Jantunen, Description and demonstration of the expolis simulation model: two examples of modeling population exposure to particulate matter, Journal of Exposure Science and Environmental Epidemiology 13 (2003) 87–99.
[39] P. E. Hart, N. J. Nilsson, B. Raphael, A formal basis for the heuristic determination of minimum cost paths, Systems Science and Cybernetics 4 (1968) 100–107.
[40] P. Dutta, P. M. Aoki, N. Kumar, A. Mainwaring, C. Myers, W. Willett, A. Woodruff, Demo abstract: Common sense: participatory urban sensing using a network of handheld air quality monitors, in: Proceedings of the 7th International Conference on Embedded Networked Sensor Systems (SenSys), ACM, 2009, pp. 349–350.
[41] D. Hasenfratz, O. Saukh, S. Sturzenegger, L. Thiele, Participatory air pollution monitoring using smartphones, in: Proceedings of the 2nd International Workshop on Mobile Sensing: From Smartphones and Wearables to Big Data, 2012.
[42] Y. Zheng, T. Liu, Y. Wang, Y. Zhu, E. Chang, Diagnosing New York City's noises with ubiquitous data, in: Proceedings of the 16th International Conference on Ubiquitous Computing (UbiComp), ACM, 2014.
[43] O. Hertel, M. Hvidberg, M. Ketzel, L. Storm, L. Stausgaard, A proper choice of route significantly reduces air pollution exposure–a study on bicycle and bus trips in urban streets, Science of the Total Environment 389 (2008) 58–70.
[44] M. H. Sharker, H. A. Karimi, Computing least air pollution exposure routes, International Journal of Geographical Information Science 28 (2014) 343–362.
[45] D. Allemann, M. Raubal, Towards health-optimal routing in urban areas, in: Proceedings of the 2nd International Workshop on HealthGIS, ACM, 2013.